

Resonant Tidal Disruption in Galactic Nuclei

Kevin P. Rauch¹ and Brian Ingalls

Canadian Institute for Theoretical Astrophysics,
University of Toronto,
60 St. George St., Toronto, On M5S 3H8, Canada.

ABSTRACT

It has recently been shown that the rate of angular momentum relaxation in nearly-Keplerian star clusters is greatly increased by a process termed resonant relaxation (Rauch & Tremaine 1996); it was also argued, via a series of scaling arguments, that tidal disruption of stars in galactic nuclei containing massive black holes could be noticeably enhanced by this process. We describe here the results of numerical simulations of resonant tidal disruption which quantitatively test the predictions made by Rauch & Tremaine. The simulation method is based on an N -body routine incorporating cloning of stars near the loss cone and a semi-relativistic symplectic integration scheme. Normalized disruption rates for resonant and non-resonant nuclei are derived at orbital energies both above and below the critical energy, and the corresponding angular momentum distribution functions are found. The black hole mass above which resonant tidal disruption is quenched by relativistic precession is determined. We also briefly describe the discovery of chaos in the Wisdom-Holman symplectic integrator applied to highly eccentric orbits and propose a modified integration scheme that remains robust under these conditions.

We find that resonant disruption rates exceed their non-resonant counterparts by an amount consistent with the predictions; in particular, we estimate the net tidal disruption rate for a fully resonant cluster to be about twice that of its non-resonant counterpart. No significant enhancement in rates is observed outside the critical radius. Relativistic quenching of the effect is found to occur for hole masses $M > M_Q = (8 \pm 3) \times 10^7 M_\odot$. The numerical results combined with the observed properties of galactic nuclei indicate that for most galaxies the resonant enhancement to tidal disruption rates will be very small.

Subject headings: black hole physics — galaxies: active — galaxies: nuclei — stellar dynamics

¹Current Address: Dept. of Astronomy, University of Maryland, College Park, MD 20742-2421.

1. Tidal Disruption in Galactic Nuclei

1.1. Introduction

It has long been speculated that massive black holes (MBHs) reside in the centers of many or most galaxies (e.g., Lynden-Bell 1969)—a notion strongly supported by recent high-resolution observations of galactic nuclei (Eckart & Genzel 1996; van der Marel et al. 1997; Kormendy et al. 1996; Kormendy & Richstone 1995 and references therein); these observations also indicate that the density of stars rises continuously towards the center of the galaxy. It is nearly certain, therefore, that tidal disruption of stars by central MBHs actively occurs in many galaxies.

Possible observable consequences of tidal disruption in galactic nuclei have been proposed by numerous authors. Hills (1975) first suggested that the ultimate power source for active galactic nuclei (AGNs) might be the accretion onto an MBH of gas from tidally disrupted stars (cf. the related model by Stoeger, Pacholczyk, & Stepinski 1992). Although subsequent calculations (Frank 1978; McMillan, Lightman, & Cohn 1981; Duncan & Shapiro 1983) showed that this mechanism was incapable of sustaining typical AGN luminosities—the stellar densities and dispersions required implied that physical collisions would dominate the mass loss—tidal disruptions may nonetheless contribute significantly to the luminosity of some AGNs, particularly the less energetic variants such as Seyferts and LINERs (low ionization nuclear emission line regions). The X-ray outbursts observed in some Seyfert-like nuclei (Grupe et al. 1995; Bade, Komossa, & Dahlem 1996), for example, could be the result of tidal disruptions. Additional observations that can be understood in terms of stellar disruptions include the variations in the strength and profile of Balmer lines seen in the Seyfert/LINER NGC 1097 (Storchi-Bergmann et al. 1995) and other active nuclei (Eracleous et al. 1995), and the absence of compact nuclear UV sources in $\sim 80\%$ of a sample of LINERs (Eracleous, Livio, & Binette 1995). The latter, for instance, was interpreted using a ‘duty cycle’ model in which the emission line region is powered by episodic accretion events (produced by tidal disruptions) lasting a few decades each but active only $\sim 20\%$ of the time on average. A model by Roos (1992) hypothesizes that broad-line clouds in AGNs are the remnants of tidal disruptions. It has also been suggested that the shell-like structure Sgr A East in the Galactic Center region may be the result of a disruption event occurring $\sim 10^4$ yr ago (Khokhlov & Melia 1996). Other possible signatures of tidal disruptions include transient flares in otherwise quiescent nuclei (Rees 1988), high-velocity stars produced by tidal dissociation of binaries (the other star being left bound to the MBH; Hills 1988; Hills 1991), and nuclear enrichment in particular isotopic species due to the explosive nucleosynthesis which might occur in relativistic disruption events (Luminet & Barbuy 1990). It has even been suggested (Carter 1992) that cosmological γ -ray bursts could be the result of extreme

disruption events in distant nuclei.

Research into tidal disruption can be divided into two classes: studies of the dynamics of the tidally disrupted debris itself, and studies of the disruption-induced dynamical evolution of the nuclear star cluster. The former has been investigated by several groups (e.g., Carter & Luminet 1983; Evans & Kochanek 1989; Laguna et al. 1993; Kochanek 1994), their most basic finding being that approximately half of the disrupted debris remains bound to the hole (and is eventually accreted) with the remainder being ejected from the nucleus. In this paper we undertake an analysis of the latter type: an investigation of loss cone dynamics under the influence of resonant relaxation (Rauch & Tremaine 1996, hereafter RT96), an enhancement to two-body relaxation that is especially pronounced in nearly-Keplerian stellar systems.

Unless explicitly overridden, we will employ geometric units throughout this paper. In these units, $G = c = M = 1$ (where M is the hole mass) and the natural units of time, distance, and angular momentum are GM/c^3 , GM/c^2 , and GM/c , respectively.

1.2. Review of Non-Resonant Loss Cone Dynamics

The contribution of tidal disruptions driven by two-body relaxation to the dynamical evolution of star clusters has been examined in detail (Frank & Rees 1976; Lightman & Shapiro 1977; Shapiro & Marchant 1978; Cohn & Kulsrud 1978). The loss cone itself can be defined as the region of phase space for which the periapsis of the stellar orbit, r_p , lies inside the star’s tidal radius, $r_t \approx 2(M/m_*)^{1/3}R_*$; these orbits are normally highly radial. Restated in terms of angular momentum, loss cone orbits are those with $L < L_{\min}$, where $L = [a(1 - e^2)]^{1/2}$ is the angular momentum of a Keplerian orbit with semi-major axis a and eccentricity e , and $L_{\min} = [(2 - r_t/a)r_t]^{1/2} \approx (2r_t)^{1/2}$ is the angular momentum of an orbit with periapsis $r_p = r_t$. It is useful to define a parameter $q = (\Delta L_{\text{orb}}/L_{\min})^2$, where ΔL_{orb} is the rms change in angular momentum (due to two-body relaxation) per orbital period; there are then two limiting cases to consider. For $q \ll 1$, stars take many orbital periods to diffuse across the width of the loss cone and hence stars entering the loss cone disrupt within an orbital period; this is the “empty loss cone” or “diffusion” limit in which the phase space density drops exponentially (with scale length $\sim \Delta L_{\text{orb}}$) in the region $L < L_{\min}$. For $q \gg 1$, stars can relax across the loss cone in less than an orbital period and thus only a fraction $\sim 1/q$ of the stars crossing the loss cone are disrupted (recall that L -space is effectively two dimensional in this problem); this is the “full loss cone” or “pinhole” limit for which the loss cone is dynamically unimportant and phase space densities inside and outside the loss cone are nearly equal. Since $L_{\min} = L_{\min}(\mathcal{E})$ and $\Delta L_{\text{orb}} \approx \Delta L_{\text{orb}}(\mathcal{E})$ (where $\mathcal{E} = 1/(2a) > 0$ is the orbital binding energy)—for realistic density profiles, the two-body relaxation time at

fixed \mathcal{E} depends only weakly on L — $q \approx q(\mathcal{E})$ and one can define a “critical energy,” $\mathcal{E}_{\text{crit}}$, for which $q(\mathcal{E}_{\text{crit}}) = 1$. Somewhat more loosely, one can define the boundary by a critical radius $r_{\text{crit}} \sim 1/\mathcal{E}_{\text{crit}}$.

The qualitative influence of the loss cone on the overall structure of the cluster is now easy to see. For $\mathcal{E} < \mathcal{E}_{\text{crit}}$ ($r \gtrsim r_{\text{crit}}$), $q > 1$ (the enclosed cluster mass fraction is larger, orbits are less nearly Keplerian, and hence they relax relatively faster) and the loss cone has minimal effect on the distribution function, $f(\mathcal{E}, L)$. Outside the critical radius, therefore, the density profile will follow the classical $\rho_\star \propto r^{-7/4}$ profile (Bahcall & Wolf 1976; this assumes an isotropic cluster and collisionless cusp growth—cf. Quinlan, Hernquist, & Sigurdsson 1995) and the cluster will remain locally isotropic, i.e., $f(\mathcal{E}, L) \approx f(\mathcal{E})$. Conversely, for $\mathcal{E} > \mathcal{E}_{\text{crit}}$ ($r \lesssim r_{\text{crit}}$), $q < 1$ and the removal of stars by tidal disruption is significant; the density cusp begins to flatten inside r_{crit} , eventually turning over and then reaching zero at r_t (the detailed calculations indicate that the flattening inside r_{crit} begins logarithmically slowly—by $r \sim 10r_t$, the cusp slope flattens by only ~ 0.2). In addition, phase space densities at fixed energy are severely depleted at low angular momenta: $f(\mathcal{E}, L) \approx 0$ for $L < L_{\text{min}}$. For typical “cuspy” nuclear density profiles ($\rho_\star \propto r^{-\gamma}$ with $1 < \gamma < 2$, which encloses the range observed in real galaxies; Lauer et al. 1995), the total rate of disruptions is dominated by the contribution from stars with energies near $\mathcal{E}_{\text{crit}}$. The simulations of Shapiro & Marchant (1978), for example, found the mean energy of disrupted stars to be $\sim 3\mathcal{E}_{\text{crit}}$ (the *median* value, on the other hand, was near $\mathcal{E}_{\text{crit}}$).

An order of magnitude estimate for $\mathcal{E}_{\text{crit}}$ follows easily from the definition $q(\mathcal{E}_{\text{crit}}) = (\Delta L_{\text{orb}}/L_{\text{min}})^2 = 1$. First, let $L_{\text{max}} = a^{1/2}$ denote the maximum angular momentum for an orbit with semi-major axis a . Then $\Delta L_{\text{orb}}/L_{\text{max}} \sim (t_{\text{orb}}/t_r)^{1/2}$ and $L_{\text{min}}/L_{\text{max}} \sim (2r_t/a)^{1/2}$, where t_r is the two-body relaxation time (e.g., Spitzer & Hart 1971). Assuming in addition $R_\star \propto m_\star^{2/3}$, $\rho_\star \propto r^{-7/4}$, and an orbit-averaged value for t_r , we find

$$\mathcal{E}_{\text{crit}} \sim 2 \times 10^{-7} \left(\frac{m_\star}{M_\odot} \right)^{8/27} M_8^{-1/27} \rho_6^{4/9}, \quad (1)$$

where $M_8 = M/(10^8 M_\odot)$ and $\rho_6 = \rho_\star(1 \text{ pc})/(10^6 M_\odot \text{ pc}^{-3})$. In physical units, the corresponding value of $r_{\text{crit}} = 1/(2\mathcal{E}_{\text{crit}})$ is

$$r_{\text{crit}} \sim 10 \left(\frac{m_\star}{M_\odot} \right)^{-8/27} M_8^{28/27} \rho_6^{-4/9} \text{ pc}. \quad (2)$$

We will parameterize the relative importance of tidal disruption in a cluster using a dimensionless function $\lambda(\mathcal{E})$, defined to be the fraction of stars at energy \mathcal{E} consumed in the loss cone each orbital period. Let λ_0 denote the theoretical value of λ for a fully non-resonant

cluster. In the pinhole limit ($q \gg 1$), the loss cone is dynamically unimportant and λ_0 is simply the fractional area of the energy hypersurface occupied by the loss cone:

$$\lambda_0 \simeq \left(\frac{L_{\min}}{L_{\max}} \right)^2, \quad q > 1. \quad (3)$$

In the empty loss cone limit, $q \ll 1$, the loss rate can be found by solving the Fokker-Planck equation (e.g., Cohn & Kulsrud 1978), which yields

$$\lambda_0 \simeq \frac{\Delta L_{\text{orb}}^2}{L_{\max}^2 \ln(L_{\max}/L_{\min})}, \quad q < 1. \quad (4)$$

One result of our analysis will be a comparison of $\lambda(\mathcal{E})$ between equivalent resonant and non-resonant systems (§ 3.1).

1.3. Resonant Relaxation Summary

Under the usual two-body relaxation process, both the energy \mathcal{E} and angular momentum L of stellar orbits diffuse (i.e., random walk) slowly through phase space due to the mutual gravitational interactions with other stars in the cluster; on average, therefore, the variations in \mathcal{E} and L , $\Delta\mathcal{E}$ and ΔL , grow with time $\propto t^{1/2}$, and the energy and angular momentum relaxation times coincide, $t_{\mathcal{E}} \sim t_L$. As discussed in detail by RT96, resonant relaxation is a process by which angular momentum relaxation can be dramatically enhanced in clusters whose mean potential contains ‘resonant’ structure (energy relaxation is not affected). It operates most effectively in nearly-Keplerian star clusters, whose resonant structure consists of spherical symmetry and equality of the radial and azimuthal orbital frequencies. In this case, the changes in both the vector and scalar angular momenta grow approximately linearly with time—systematically faster than a random walk—and hence the angular momentum relaxation time is much shorter than the energy relaxation time: $t_L \ll t_{\mathcal{E}}$ (possibly by several orders of magnitude).

Because the nuclear cluster of every galaxy with a central MBH is nearly-Keplerian close to the black hole, resonant relaxation can have important consequences for the dynamics of galactic nuclei. Whenever $t_L < t_H < t_{\mathcal{E}}$, for instance (where t_H is the Hubble time), resonant relaxation will act to isotropize the cluster in less than the age of the universe, even though the two-body relaxation time is much longer than t_H (as is typical for galactic nuclei). In the form of resonant dynamical friction, resonant relaxation can exert a controlling influence on the eccentricity evolution of a massive black hole binary (cf. Quinlan & Hernquist 1997); it can also rapidly erode the inclination of relatively massive bodies in nearly-Keplerian disk systems. For details, see RT96.

In this paper we examine in depth another consequence of resonant relaxation: resonant tidal disruption. In RT96 it was shown that the enhanced relaxation of L should lead to a large increase of the tidal disruption rate in the empty loss cone region ($q \ll 1$), by a factor of roughly $q^{-1/2}$; since disruption rates are not enhanced in the full loss cone region, however, they estimated that the overall disruption rate would increase only moderately (a factor of two or three at most). It was also argued that relativistic precession due to the MBH should effectively disable resonant tidal disruption for hole masses $M \gtrsim 4 \times 10^7 M_\odot$. (Resonant relaxation only operates on timescales shorter than the orbital precession time, which becomes dominated by relativistic effects as the tidal radius approaches the horizon.) However, resonant relaxation is a highly non-linear phenomenon, and it is difficult for analytic calculations to achieve better than order-of-magnitude accuracy; these numerical estimates are, therefore, rather crude.

In the present work we discuss the results of detailed numerical simulations designed to quantitatively test these predictions. We calculate both the resonant enhancement to the tidal disruption rate and the associated change in the cluster distribution function. The influence of relativistic precession on the results is also investigated, yielding an improved estimate of the “quenching mass” above which resonant tidal disruption is disabled. We begin in § 2 with a description of the numerical method. Results are presented in § 3, and concluding discussion is given in § 4. Appendices A and B provide additional discussion of technical issues pertaining to the calculations.

2. Simulation Method

2.1. Numerical Strategy

Numerical simulation of resonant tidal disruption is challenging for several reasons. First is the need to use N-body techniques in a case where the physical system under study contains many millions of stars. The non-resonant investigations described in § 1.2 avoided this problem by using a continuum approximation (the Fokker-Planck equation) to calculate the dynamics; in the resonant case, however, the Fokker-Planck equation is invalid—it is based on random-walk diffusion of L , whereas resonant relaxation leads to linear growth. Although it should be possible to modify the Fokker-Planck formalism to accurately account for resonant effects, this has not yet been accomplished; a particle-based approach is therefore required. We ease the computational demands by differentiating stars into two types, test and background (§ 2.2), the former serving as the tracers of dynamic evolution and the latter representing the mass responsible for driving that evolution. Further reduction in computational effort was achieved using a specialized mass spectrum (and associated soft-

ening length) for the background stars, which allowed fewer stars to be included at large distances without significantly changing the physical relaxation time (§ 2.3).

A second constraint is the high dynamic range needed in L -space: determining the resonant modification to the cluster distribution function, $f(L)$, requires adequately resolving f on scales $\sim L_{\min}$; in galactic nuclei, however, $L_{\max}/L_{\min} \sim 10^5$ for $r \sim r_{\text{crit}}$. We deal with this problem in two ways: first, by restricting the simulations to a manageable subregion of L -space defined by $L < L_0$, where $L_{\min} \ll L_0 \ll L_{\max}$; and second, by *cloning* stars approaching $L = L_{\min}$ to help reduce statistical fluctuations in this sparsely populated region of phase space (§ 2.4). Note that attempting to utilize a Fokker-Planck approach would also be complicated by these low phase space densities present near the loss cone; previous studies, by contrast, treated the loss cone as a boundary layer instead of resolving it explicitly.

The radial dynamic range of the test orbits also places stringent demands on the choice of integrator—another consequence of the extreme mismatch between L_{\min} and L_{\max} , which implies that loss cone orbits are highly radial (in our simulations, $e \gtrsim 0.9999$). As discussed in § 2.4, finding a suitable integration scheme proved an arduous task; although itself not trouble-free, the Wisdom-Holman symplectic mapping (Wisdom & Holman 1991; this scheme is also known as the mixed-variable symplectic method) emerged as the clear winner. A slightly modified form of this method, which we term “semi-relativistic” symplectic integration, was used in simulations examining the influence of general relativity on resonant tidal disruption.

A cornerstone of our analysis is the use of *comparative* simulations—i.e., simulations that were strictly identical apart from the strength of resonant effects—to determine the importance of resonant tidal disruption in a particular system. This ‘differential measurement’ approach removes as much as possible any systematic biases that may be introduced by the abstractions used to keep the problem computationally tractable. In any event, the relatively good agreement between the theoretical and measured values of quantities such as $\mathcal{E}_{\text{crit}}$ (§ 3.1) indicate that such systematic effects are probably small.

2.2. Model Overview

The basic computational model contained only two components: a central black hole and the surrounding nuclear cluster. Most simulations treated the black hole as a Newtonian point mass; those including relativistic corrections (§ 3.2) assumed a Schwarzschild geometry. In both cases the black hole was held fixed at the center of the cluster—i.e., we neglect the

Brownian motion of the hole, which is dynamically unimportant in these systems (see § 4). Black hole masses in different simulations ranged from 10^6 to $10^8 M_\odot$ (in the range of those inferred from observations) and remained fixed for the duration of the run—i.e., we neglect any evolution of the black hole due to accretion of tidal debris.

The nuclear cluster was modeled as a halo of bound, $1 M_\odot$ stars with a distribution function of the form $f(\mathcal{E}) \propto \mathcal{E}^{1/4}$ for $\mathcal{E}_{\min} \leq \mathcal{E} \leq \mathcal{E}_{\max}$, and $f(\mathcal{E}) = 0$ elsewhere—in other words, as an isotropic cusp with a radial density profile $\rho_\star \propto r^{-7/4}$ in the range $a_{\min} \lesssim r \lesssim a_{\max}$, where $a_{\min} = 1/(2\mathcal{E}_{\max})$ and $a_{\max} = 1/(2\mathcal{E}_{\min})$ are the corresponding semi-major axes; this is the Bahcall & Wolf (1976) solution, valid for $r \gg r_t$ (see § 1.2). On physical grounds, $a_{\min} \gtrsim r_t$ and $a_{\max} \lesssim r_h$ are required, where r_h ($\sim 1/\sigma^2$ for a cluster with velocity dispersion σ) is the black hole’s dynamical sphere of influence, outside of which the cusp solution need not apply. In practice, a_{\min} and a_{\max} were restricted to a narrower band centered on r_{crit} in order to minimize the number of simulated stars; typical values were $a_{\min} \sim r_{\text{crit}}/30$ and $a_{\max} \sim 10 r_{\text{crit}}$. The absolute density was chosen to keep the mass fraction small at the critical radius, a requirement for resonant relaxation to be effective there; in most cases, $\rho_\star(1 \text{ pc}) \sim 10^3 M_\odot \text{ pc}^{-3}$ was used. Typical galactic nuclei have $\rho_\star(1 \text{ pc}) \sim 10^4\text{--}10^6 M_\odot \text{ pc}^{-3}$ (cf. § 4).

Although the use of N-body techniques in our simulations was mandatory (§ 2.1), a fully self-consistent N-body integration would have been wasteful; since there is minimal dynamical evolution of the nucleus as a whole during the course of the simulations, following the detailed trajectory of every cluster star is unnecessary. For this reason the simulations separated the cluster into two types of stars, test and background, according to the treatment of their dynamical evolution.

Conceptually the background stars represent the mass of the cluster, providing the perturbing force felt by the test stars; the test stars, by contrast, are the dynamic tracers of the cluster’s equilibrium distribution and tidal disruption rate. Hence only the test stars’ dynamical evolution is considered—they feel the forces of the black hole and the background stars (but not of the other test stars), and their orbits relax nearly as they would in a fully self-consistent integration; background stars feel only the central force and execute unperturbed Keplerian motion for the duration of the simulation. If there are n test stars and $N \gg n$ background stars, the force calculation in this scheme is then $O(nN)$ instead of the much larger $O((n + N)^2)$ for a self-consistent calculation. The detailed handling of each is explained in the following sections.

2.3. Background Cluster Specifics

Given a_{\min} , a_{\max} , and $\rho_6 \equiv \rho_{\star}(1 \text{ pc})/(10^6 M_{\odot} \text{ pc}^{-3})$, the number of background stars, N , is known. Even at the rather low simulated densities, however, there were too many background stars to include individually—most clusters having $N \sim 10^5 - 10^6$ and the practical limit being a few thousand. The simplest solution to this problem would be to increase the mass of every background star in proportion to their total overabundance; we adopted a more flexible strategy in which mass was made a function of the star’s (constant) semi-major axis, the most massive “stars” occupying the largest, most distant orbits. This approach allowed the background cluster to retain both its fine-grained structure at small radii, where average interstellar distances are shortest, and its overall mass, which is dominated by the stars at large radii. The original mass density profile was preserved by concomitantly decreasing the stellar *number* density at large radii. More precisely, the background stars were given a mass spectrum of the form

$$\tilde{m}(a) = \begin{cases} m_{\star}, & a_{\min} \leq a \leq a_c; \\ m_{\star}(a/a_c)^{5/4}, & a_c \leq a \leq a_{\max}. \end{cases} \quad (5)$$

In addition, for $a > a_c$ their number density was forced to be $\propto r^{-3}$, resulting in a mass density $\propto r^{-7/4}$ at all radii, as desired; for $a < a_c$, stars had their nominal mass and a number density $\propto r^{-7/4}$. The initial orbital velocities of the more massive stars were also given a moderate tangential bias to prevent these masses from reaching small radii, where they would severely skew the local density; otherwise the orbits were drawn isotropically. The value of a_c was determined by the requirement that \tilde{N} masses, drawn at random from the above distribution, have (on average) a combined mass equal to that of the actual cluster ($= m_{\star}N$), where \tilde{N} was the number of background masses to include in the simulation; most runs used $\tilde{N} = 2000$. All simulations used $m_{\star} = 1 M_{\odot}$.

Another consideration in setting up the background cluster was the amount by which to soften the point mass potentials of the background stars, which is necessary with constant timestep integrators (such as the Wisdom-Holman mapping) to maintain accuracy during close encounters (see § 2.4 below). Note first that using equal softening lengths for all stars is impractical—the background masses spanned several decades in radius, and using the same softening length for each would produce either negligible softening for the outermost masses or excessive softening for the innermost. We therefore decided to use a softening length proportional to the semi-major axis of the orbit. The more massive stars, however (those with $a > a_c$), were treated a bit differently in this regard. Because they actually represent a group of discrete stars which have been condensed into a single mass for computational efficiency (a type of “poor man’s tree code”), the softening length for these objects should take account of their implied finite size; this in turn depends on their mass and average

density. Based on the specific form of $\tilde{m}(a)$, the softening length b used for a particular background mass was:

$$b(a) = 0.02a \times \begin{cases} 1, & a_{\min} \leq a \leq a_c; \\ 5a/(4a_c + a), & a_c \leq a \leq a_{\max}. \end{cases} \quad (6)$$

Thus $b \approx 0.1a$ for $a \gg a_c$, which provided a good fit to the actual mean potential of the massive stellar aggregates. In terms of b the softened potential was $\Phi = -\tilde{m}/(r^2 + b^2)^{1/2}$.

Finally, we comment on how the orbital integrations for the background stars were performed. As mentioned earlier the background stars follow strictly Keplerian orbits, and hence their orbital motion can be calculated analytically. If the integration timestep is small enough, however, direct integration will be faster since one analytic Kepler step is an order of magnitude slower than one direct step. To maximize efficiency, the code therefore used direct integration whenever a few such steps would yield sufficient accuracy; otherwise orbits were advanced analytically. Direct integrations employed a second-order leapfrog step which maintained a relative energy accuracy of $\lesssim 10^{-3}$ at all times.

2.4. Test Star Integrations

Because of the special demands on the test star integrator (§ 2.1), we tested the relative performance of a wide variety of methods, including both direct integration schemes (such as leap frog, adaptive Runge-Kutta, and Bulirsch-Stoer) applied to either the ordinary or regularized equations of motion and specialized schemes (such as Ecke’s method and the mixed-variable symplectic method) which model the motion as a perturbed Keplerian ellipse. The latter have the advantage of being able to use relatively large step sizes for particles undergoing nearly-Keplerian motion, as is true of the test stars. Symplectic integrators have the advantage that they are normally free of long-term growth of energy error, but only if a constant stepsize is used—hence they also have the disadvantage of being non-adaptive. As the extreme orbital eccentricities in this problem demand that the integrator be (in some sense) adaptive, non-adaptive direct methods such as leap frog or its higher-order variants were completely unusable. In the end none of the direct schemes proved to be competitive with the specialized ones. Of the two methods of the latter type, Encke’s method turned out to be surprisingly inferior to the mixed-variable symplectic (hereafter, MVS) method, particularly since only the former can utilize an adaptive stepsize. Encke’s method (e.g., Danby 1992) works by recasting the equations of motion in terms of deviations from a fixed Keplerian reference orbit that is periodically reset (once per orbit, say). In theory, since these deviations are normally small and slowly-varying for nearly-Keplerian motion they can be integrated more easily than the original equations; in the limit of unperturbed Keplerian

motion the deviations remain precisely zero and the method is exact for arbitrarily large stepsizes. The MVS method (Wisdom & Holman 1991; cf. Kinoshita, Yoshida, & Nakai 1991) can be thought of either as a symplectic analog of Encke’s method in which the reference orbit is reset every time step, or (better) as a specialization of the leap frog step in which the rectilinear motion between the impulsive velocity changes is replaced by a Keplerian orbital segment; this method is also exact in the limit of unperturbed Keplerian motion. Our testing highlighted the fact that even if the absolute deviations integrated by Encke’s method remain small, their *derivatives* can vary sharply—mainly near periapse. This implies that the deviation equations must be very carefully integrated when passing periapse, requiring the use of extremely small stepsizes for highly eccentric orbits; this probably explains the method’s poor performance in our problem. We therefore chose to use the MVS method for our calculations. Not even this scheme was problem-free, however, as it was found to inject a (remarkably!) large amount of spurious energy relaxation into the motion. Appendix B discusses the origin of this behavior (which appears to be dynamical chaos in the MVS integrator) as well as the workaround we used to mitigate the problem. The final simulations were not adversely affected by the malady. A fringe benefit of the MVS scheme is the ease with which tidal disruptions can be detected; since the spatial motion between velocity perturbations is purely Keplerian, the minimum radius crossed during each step can be efficiently determined.

As noted previously it was impractical to simulate all of L -space in our calculations—even resonant relaxation is too slow for this to be computationally feasible with N-body methods. We therefore focussed attention on a more manageable region of phase space around the loss cone, only considering test orbits with angular momenta $L < L_0$, where $L_{\min} \ll L_0 \ll L_{\max}$. Our estimates of the resonant modification to $f(L)$ is thus confined to $L < L_0$; since resonant effects are most dramatic near L_{\min} , however, this was not a significant restriction (see § 3). There is, of course, nothing physically special about this boundary, and test stars inside the simulation boundary will freely relax across it unless manually restricted. We implemented this restriction by considering $L = L_0$ to be a *reflecting* boundary—stars crossing outside $L = L_0$ were simply removed from the simulation and replaced by *clones* (explained below) crossing the boundary towards the inside. In most simulations, $L_0 \gtrsim 10 L_{\min}$ was attainable.

To adequately resolve $f(L)$ across the entire $L < L_0$ subspace, the region was divided into a number of non-overlapping zones spaced logarithmically in L (typically ~ 20), each covering a factor of $\sim \sqrt{2}$ in L . Determining $f(L)$ (for a fixed energy \mathcal{E}) was done by integrating a population of test stars, each with initial orbital energy \mathcal{E} , until they achieved dynamic equilibrium; $f(L)$ was then determined by computing the average occupancy of each zone (weighted by their relative areas).

The small relative areas enclosed by the innermost zones makes them subject to large statistical uncertainties (i.e., Poisson noise) due to the very small average occupancies within these zones. To achieve comparable relative errors in all zones, we introduced *cloning* of test stars into the simulations, which attempts to equalize the absolute occupancies between zones by duplicating stars entering the innermost zones. Conceptually our cloning procedure is very similar to that used by Shapiro & Marchant (1978) in their Monte Carlo loss cone simulations; it differs in that whereas their cloning occurred in energy space (allowing $f(\mathcal{E})$ to be determined well above the critical energy, $\mathcal{E}_{\text{crit}}$), ours is done in L -space. The cloning process proceeded as follows. At the start of a simulation a number of zones were designated ‘ n -tuple cloning zones,’ meaning that any test star relaxing into such a zone from above (i.e., from an adjacent orbit with larger L) was replicated n times; subsequently, the n clones were integrated precisely like non-clones, except that any clone passing outside the zone in which it was created was removed from the simulation. Clones were, however, free to relax inwards (i.e., towards more radial orbits with smaller L)—possibly creating clones of their own, and so on; those suffering tidal disruption were also removed without being replaced. Disrupted *non-clones*, on the other hand, were replaced by new test stars lying just inside the reflecting boundary. Note that although the number of clones is dynamic, the number of non-clones (and thus the average test star “potential”) remains fixed. The system is therefore dynamically closed and the zonal occupations come into statistical equilibrium after a few crossing times. (Recall that since test stars do not feel the gravitational forces of the other test stars, cloning introduces no dynamical feedback into the system.) We found that great care was needed in creating the clones to avoid biasing the calculated distribution function. In particular, by construction all stars undergoing cloning have $dL/dt < 0$ (their orbits became more radial during the preceding integration step), and not only must the newly-created clones share this property, the distribution of their dL/dt values must match that of the uncloned stars. In practice this was achieved by creating candidate clones, integrating them *backwards* one timestep, and rejecting any that did not cross the cloning boundary during this step (as the original star had); otherwise the only physical variables the clones had in common with their parents were their energies \mathcal{E} and (scalar) angular momenta L .

We tested the reflection and cloning schemes by performing a preliminary simulation in which tidal disruption was artificially turned off (by simply not checking for it). Since the perturbing potential provided by the background cluster is nearly isotropic, in equilibrium the test stars should exhibit a flat distribution function, $f(L) = \text{const}$. The calculated $f(L)$ was constant to within $\approx 3\%$, which is less than the statistical uncertainty of the results presented in § 3. Other checks—e.g., that the mean density profile of the background cluster was indeed $\propto r^{-7/4}$ —were also done and all returned nominal results.

3. Results

The consequences of resonant tidal disruption were examined through a series of comparative resonant and non-resonant simulations that were otherwise identical. The non-resonant results corresponding to a particular resonant simulation were created by redoing the resonant run while artificially adding orbital precession (amounting to ~ 1 rad per orbit) to the test stars’ motion to force the precession time down to only a few orbital periods, which is short enough to extinguish resonant effects; operationally this was done by adding a small amount of precession each integration step. This technique allowed a “differential measurement” of the disruption rates and equilibrium distributions to be made, which is more robust and reliable than attempting to calibrate and match absolute results obtained from only qualitatively-similar runs.

3.1. Newtonian Simulations

This set of simulations was designed to explore the gross differences in disruption rates and dynamical equilibrium between resonant and non-resonant clusters. The runs used a hole mass $M = 10^6 M_\odot$, a value appropriate for small galactic nuclei such as the Galactic Center or M32 (cf. Table 2). In this case, $r_t \sim 100$ is well outside the horizon and relativistic effects are unimportant; hence these simulations were performed within an entirely Newtonian framework using the standard MVS algorithm.

The main simulations consisted of four sets of comparative runs, each at a fixed orbital energy; three of the four were at an energy above the critical energy, where resonant enhancements should be prominent. Phase space parameters for these calculations are shown in Table 1. The table lists the orbital energy of the test stars, \mathcal{E} , the maximum angular momentum followed in the simulation, L_0 (i.e., the location of the reflecting boundary—see § 2.4), the maximum possible angular momentum at the given energy, L_{\max} , the average amount of momentum relaxation suffered per orbit, ΔL_{orb} , and the typical relaxation suffered by resonantly relaxed stars over a full precession time, ΔL_{prec} ; subscripts “res” and “nr” refer to the values for resonant and non-resonant runs, respectively. Also given are the results for the normalized tidal disruption rates, λ , with estimated $1 - \sigma$ errors given in parentheses (λ_0 is the ‘baseline’ expectation; see § 1.2). The background cluster in these simulations had parameters (§ 2.3) $\tilde{N} = 2000$, $\rho_6 = 10^{-3}$ ($\rho_\star \propto r^{-7/4}$), $\mathcal{E}_{\min} = 2 \times 10^{-9}$, and $\mathcal{E}_{\max} = 5 \times 10^{-7}$; it was also found empirically to have $\mathcal{E}_{\text{crit}} \approx 2 \times 10^{-8}$, in good agreement with the estimate given in eq. (1).

The strong resonant enhancement to the local disruption rate is clearly evident in Ta-

ble 1. To within the accuracy of the results ($\sim 25\%$ at $1 - \sigma$), the ratio of the resonant to non-resonant tidal disruption rate is given simply by

$$\frac{\lambda_{\text{res}}}{\lambda_{\text{nr}}} = \begin{cases} L_{\text{min}}/\Delta L_{\text{orb}}, & \Delta L_{\text{orb}} \leq L_{\text{min}}; \\ 1, & \Delta L_{\text{orb}} \geq L_{\text{min}}. \end{cases} \quad (7)$$

This agrees qualitatively with the estimate given by RT96, and quantitatively restricts the previously undetermined numerical coefficient to be very close to unity. Combining this result with the analytic estimate for λ_{nr} (§ 1.2) implies that the overall rate of tidal disruptions in a resonant nucleus will be at most three times that for an equivalent non-resonant nucleus (note: for $\rho_* \propto r^{-7/4}$, it is easily shown that ΔL_{orb} is roughly proportional to \mathcal{E}^{-1}), and probably only a factor of two greater. The precise value depends on the density profile, the strength of resonant effects near $\mathcal{E}_{\text{crit}}$, the inner radius at which disruptions significantly deplete the cusp, and the radius at which relativistic effects become relevant.

A comparison of the equilibrium angular momentum distribution functions is shown in Figure 1, each panel corresponding to a specific value of \mathcal{E} (or ΔL_{orb} , marked); all curves have been normalized to have unit area in the range $[0, L_{\text{max}}]$. For each curve, the errorbar for the outermost point includes the overall uncertainty in normalization (resulting from the need to extrapolate the curves from L_0 to L_{max}) as well as the statistical uncertainty in the average bin occupancy, whereas the remaining points include only the latter. Uncertainty in the normalization of the resonant curves was estimated by splitting the difference between two extreme assumptions for how to extrapolate $f(L)$, namely: (1) $f(L) = \text{const.} = f(L_0)$, or (2) $df/d(\ln L) = \text{const.} = df/d(\ln L)_{\text{nr}}$ for $L > L_0$. Note that in agreement with previous studies, the non-resonant $f(L)$ are well fit by a straight line in semi-log coordinates (outside the loss cone); for these curves the extrapolation error was taken to be the formal uncertainty in the corresponding linear least-squares fit. The strong resonant increase in phase space density near the loss cone (which disappears outside the critical radius) is again clearly visible.

Figure 2 compares the resonant (solid) and non-resonant (dotted) $f(L)$ for a run with $L_0 \sim L_{\text{max}}$; a linear least-squares fit to the latter (dashed line) is also plotted. The figure suggests that for large L the two curves are essentially equal—the resonant enhancement becoming significant only near the loss cone. This behavior can be understood qualitatively as follows. Recalling that even resonant relaxation proceeds as a random walk on timescales longer than the orbital precession time (§ 1.3), one would expect relaxation over distances much larger than ΔL_{prec} —the effective mean free path in L -space—to proceed at almost identical rates in both resonant and non-resonant systems; their distribution functions should therefore be nearly coincident in this region. Near the loss cone, on the other hand (i.e., for $L \lesssim \Delta L_{\text{prec}}$), the effective diffusion in the resonant cluster is much higher; here, therefore, the

resonant $f(L)$ will be flatter than its non-resonant counterpart, and hence will increasingly dominate over the latter as the loss cone is approached. Inside the loss cone both curves fall exponentially with a scale length of ΔL_{orb} . This line of reasoning explains the gross features visible in Figure 2; in particular, note the apparent turnover in f_{res} for $L \gtrsim 3L_{\text{min}}$ (this particular simulation had $\Delta L_{\text{prec}} \sim 2L_{\text{min}}$).

3.2. Relativistic Simulations

We examined the importance of relativistic precession through two series of simulations. In each series, the value of $\Delta L_{\text{orb}}/L_{\text{min}}$ was held fixed while the black hole mass was varied between relatively small values, for which relativistic effects were negligible, and larger masses for which they dominated the precession. The relativistic simulations were performed in a conceptually simple manner—by merely replacing the Kepler stepper used in the usual MVS scheme (§ 2.4) with one integrating motion in the Schwarzschild (non-rotating black hole) spacetime. This is equivalent to including the relativistic corrections to the Newtonian black hole (i.e., point mass) potential in the “unperturbed motion” part of the symplectic integrator instead of in the perturbation potential. Although straightforward, this approach does not treat time dilation effects completely accurately—time is still considered an absolute, universal quantity. Since such effects are noticeable only during the extremely brief passage through periapse, however, they can be safely neglected in our case. (In fact, our method is probably overkill; artificially adding precession at the relativistic rate would likely have been sufficient.) Because of this comingling of formalisms, we refer to this scheme as “semi-relativistic” symplectic integration; for details on implementation of the Schwarzschild stepper (which incorporates a high-order approximation to geodesic motion in the Schwarzschild metric) see Appendix A.

Figure 3 displays the disruption rate λ as a function of black hole mass for test stars undergoing strongly resonant relaxation ($\Delta L_{\text{orb}}/L_{\text{min}} = 0.025$) in the non-relativistic case. The points $\lambda(M \rightarrow 0)$ and $\lambda(M \rightarrow \infty)$ correspond to purely Newtonian resonant and non-resonant simulations, respectively. The figure shows very clearly the quenching effect of relativistic precession at large hole masses: whereas the scale-free Newtonian simulations predict a factor of ≈ 30 enhancement in the tidal disruption rate due to resonant effects (cf. Table 1), for a physical hole mass of (say) $10^6 M_{\odot}$, the relativistic simulations show only a factor of ≈ 5 net increase. The “quenching mass” at this energy is thus approximately $10^6 M_{\odot}$. Near the critical energy, on the other hand, relativistic effects from a $10^6 M_{\odot}$ black hole would not noticeably wash out the (much smaller, but more robust) resonant enhancement to λ ; accomplishing this requires a much shorter precession period—and hence

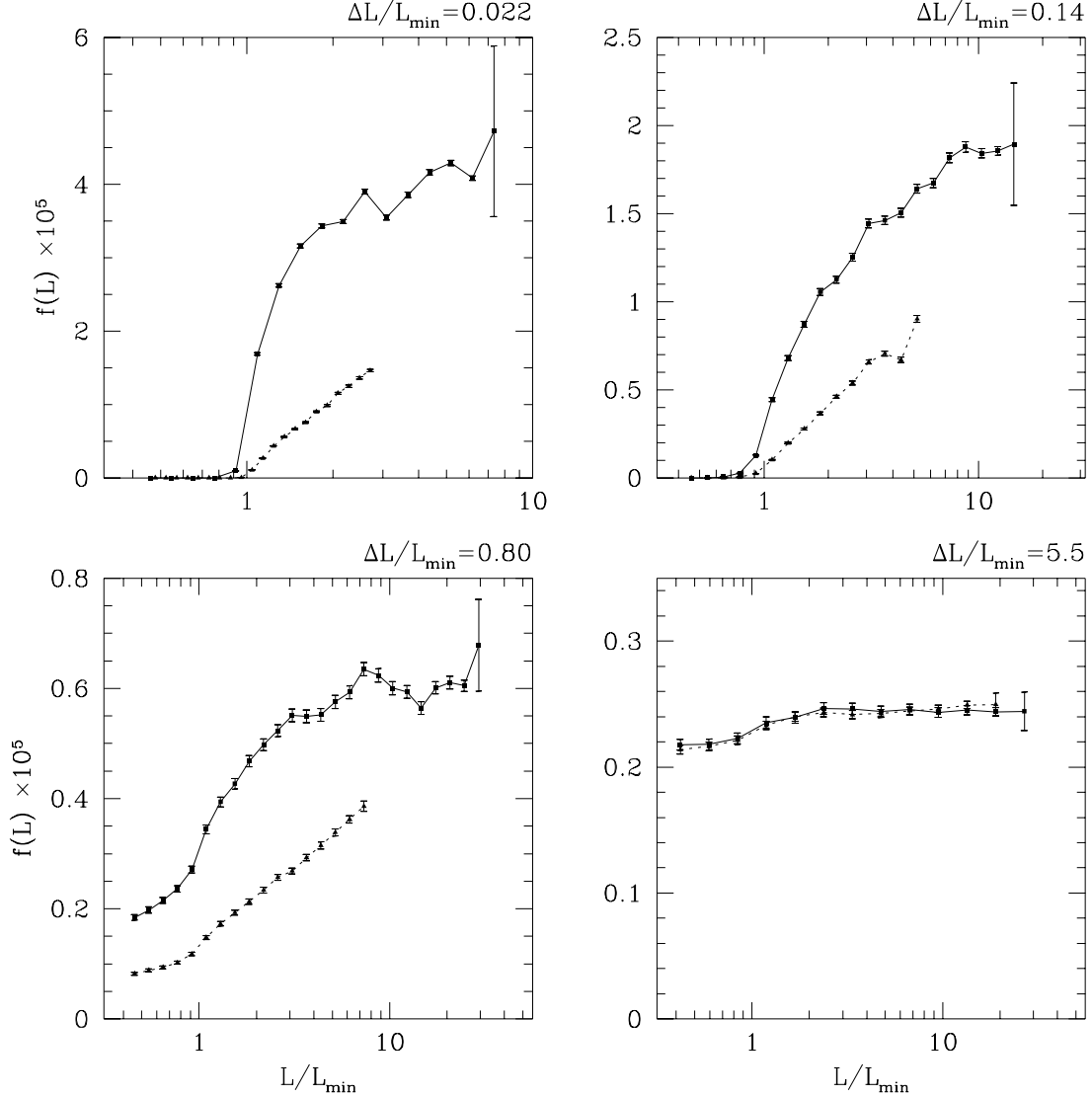


Fig. 1.— A comparison at several energies of the normalized L -space distribution functions, including approximate $1\text{-}\sigma$ error bars, for equivalent resonant (solid curves with square points) and non-resonant (dotted curves with triangular points) clusters. The large, outermost error bars include the uncertainty in overall normalization; the remainder show only the formal statistical uncertainties in each point. In the empty loss cone limit, $\Delta L_{\text{orb}}/L_{\text{min}} \ll 1$, resonant phase space densities are much higher near the loss cone, implying a large increase in the local tidal disruption rate relative to non-resonant clusters (cf. Table 1).

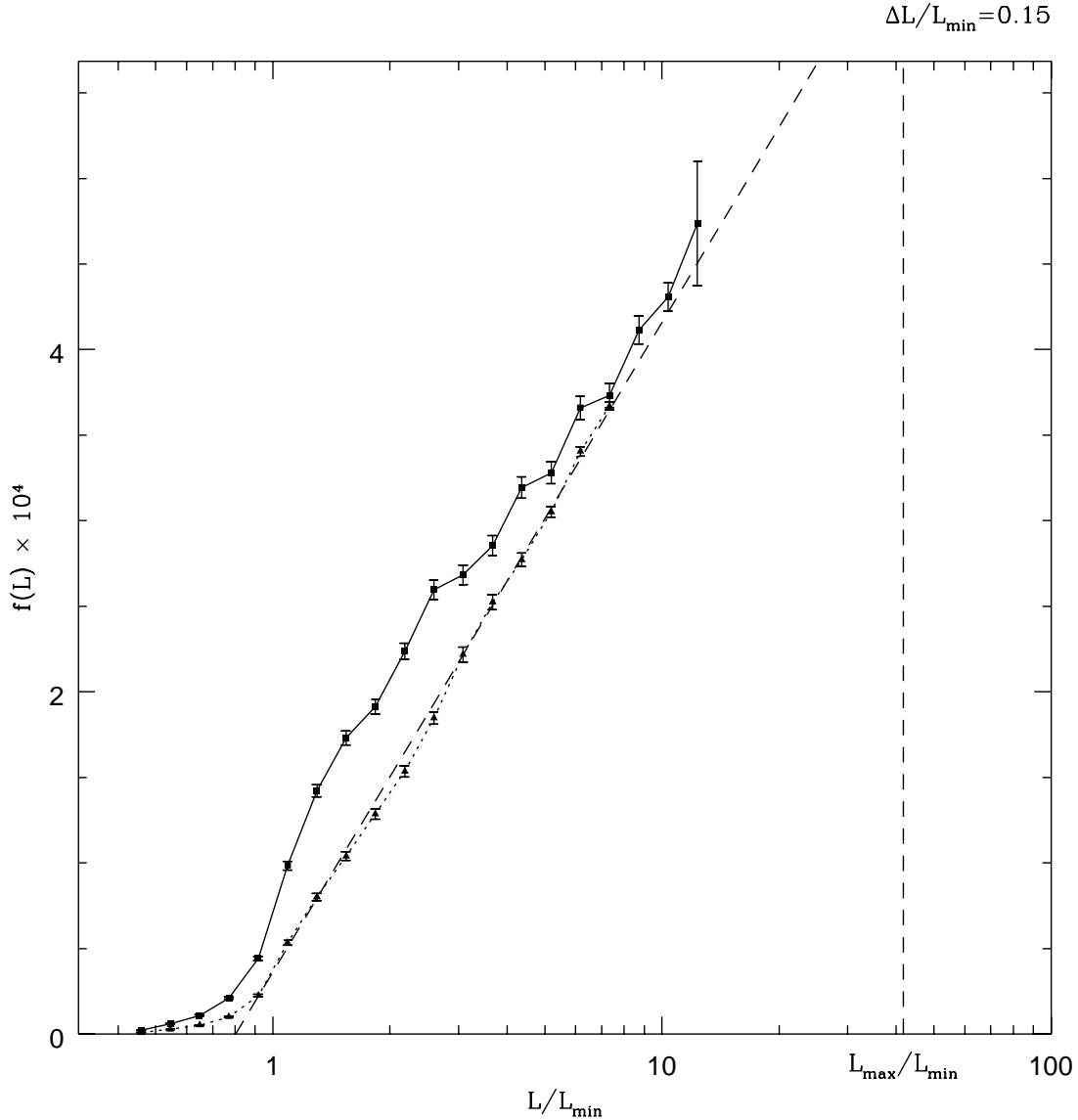


Fig. 2.— A comparison of resonant (solid curve with square points) and non-resonant (dotted curve with triangular points) distribution functions near L_{\max} (marked). The dashed line through the non-resonant $f(L)$ is a linear (in semi-log coordinates) least-squares fit to the data. For $L \gg \Delta L_{\text{prec}} \sim 2$, the two curves appear to merge; only nearer the loss cone is the resonant enhancement to $f(L)$ significant.

a larger black hole.

The second set of relativistic simulations were designed to estimate the hole mass above which all resonant tidal effects disappear. Three distinct groups of runs were performed, all with a fixed value of $\Delta L_{\text{orb}}/L_{\text{min}} = 0.3$: (1) non-relativistic, non-resonant; (2) non-relativistic, resonant; and (3) relativistic, resonant. We will define the quenching mass as the black hole mass for which half the total resonant enhancement to the overall tidal disruption is relativistically suppressed. In this case, the estimate is made more difficult by the relatively small resonant excess near the critical energy as well as the large array of runs required. From the results of ≈ 20 runs spanning hole masses of 10^7 to 10^8 , our best estimate for the quenching mass M_{Q} is

$$M_{\text{Q}} = (8 \pm 3) \times 10^7 M_{\odot}. \quad (8)$$

This is also close to the rough estimate of $4 \times 10^7 M_{\odot}$ given in RT96.

4. Discussion

We have shown that resonant tidal disruption strongly enhances the disruption rate in the empty loss cone limit, by a factor of $\approx L_{\text{min}}/\Delta L$; the total disruption rate for the entire cluster is approximately double the non-resonant rate. We also found that for hole masses $M \gtrsim 8 \times 10^7 M_{\odot}$, the latter increase is eliminated by relativistic precession; sufficiently far into the diffusion limit, this quenching effect is also present for smaller black holes. These results quantitatively confirm the order-of-magnitude estimates given in RT96 and highlight the potential importance of resonant relaxation in determining the structure of galactic nuclei at small radii.

Other processes capable of modifying loss cone dynamics include black hole wander and tidal capture. Black hole wander (Lin & Tremaine 1980; Young 1977; Bahcall & Wolf 1976)—the result of two-body relaxation acting on the hole itself—is a Brownian motion-like process which causes the hole to undergo minor excursions from the true dynamical center of the nucleus. Like resonant tidal disruption, BH wander is never important in the full loss cone regime—not even the existence of a loss cone, much less its precise location, is of consequence in this case. In the empty loss cone case, BH wander can modestly enhance the local non-resonant disruption rate by a logarithmic factor (Young 1977); however, we do not expect resonant relaxation and BH wander to significantly reinforce each other in this regard. This is because resonant nuclei have relatively low densities and hence large r_{crit} ; the low velocity dispersions here then imply loss cone impact parameters $b_{\text{t}} \sim L_{\text{min}}/v \gg r_{\text{w}}$, where r_{w} is the rms BH wandering radius (even in the relatively dense Galactic Center, for

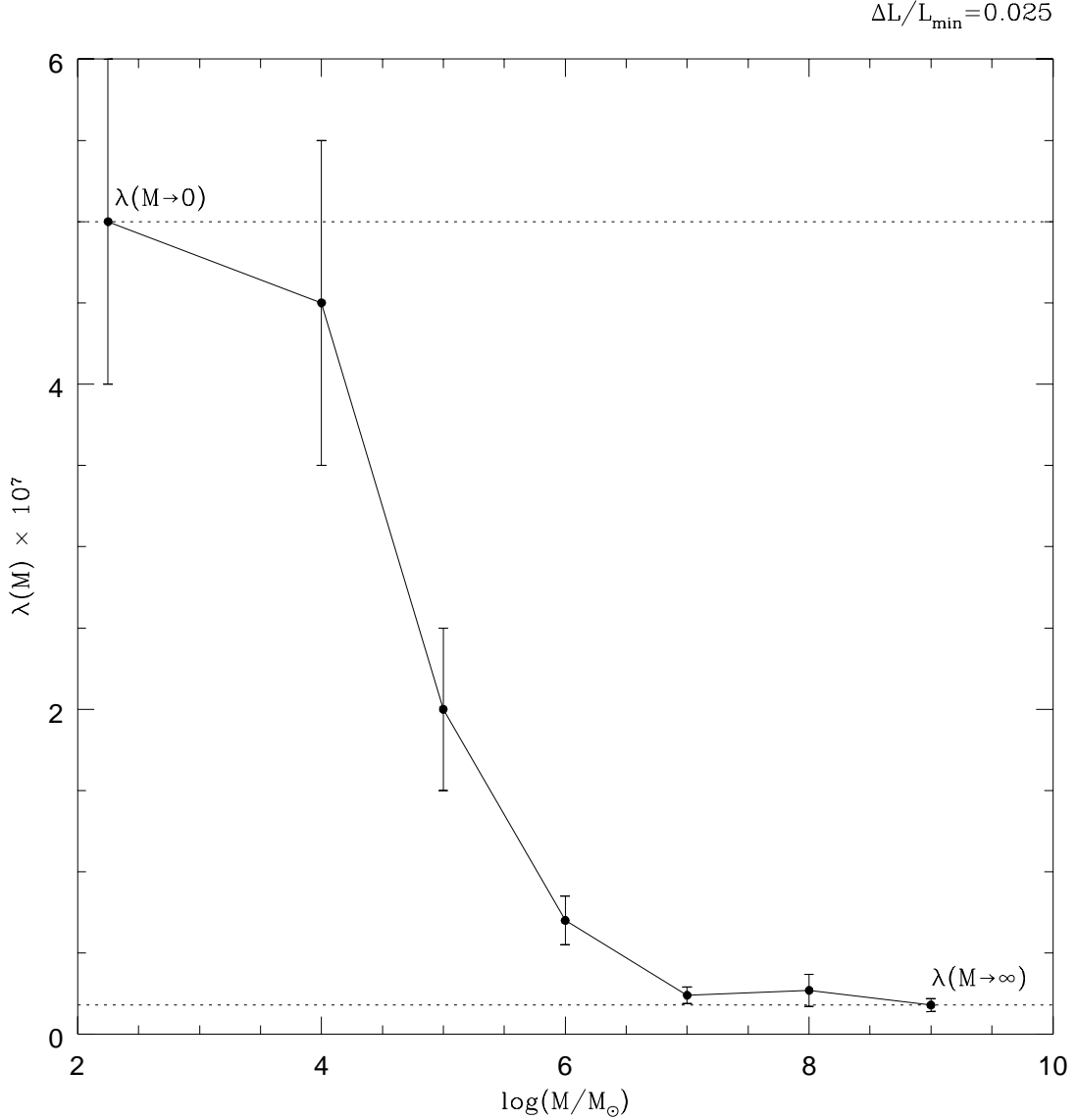


Fig. 3.— A plot of the fractional disruption rate per orbital period, λ , as a function of the black hole mass, M , for a series of otherwise identical resonant clusters. For very massive holes, the resonant enhancement to λ is quenched—the result of an increasing amount of relativistic precession near the loss cone as the tidal radius moves closer to the horizon. When relativistic precession is negligible (leftmost point), the disruption rate is ~ 30 times higher than in the corresponding non-resonant cluster (rightmost point). In this particular case, half of this increase is gone by $M \sim 10^6 M_{\odot}$; near the critical energy (where $\Delta L_{\text{orb}}/L_{\min} \sim 1$) the quenching mass is larger, $\sim 8 \times 10^7 M_{\odot}$ (see § 3.2).

example, $b_t \sim 3r_w$ near r_{crit}). At smaller radii, by contrast, the tightly bound cusp stars have orbital periods short compared to the wandering timescale, and therefore follow the hole adiabatically. There could be an intermediate region in which BH wander and resonant effects reinforce each other, but in general this does not happen.

Tidal capture, on the other hand, will further enhance resonant disruption rates just as it enhances non-resonant tidal disruption. Tidal capture (Diener et al. 1995; Novikov, Pethick, & Polnarev 1992; Rees 1988; Frank & Rees 1976) occurs when a star passes close to, but outside of, its tidal radius; although it escapes immediate destruction, the tides raised on the star dissipate enough orbital kinetic energy inside the star to substantially reduce the semi-major axis of the orbit (the pericentric distance remains nearly fixed). This process continues until either the orbit circularizes or the star disrupts; in the case of a massive black hole, the studies indicate that the latter will occur. (We remark that the consequence of tidal capture in \mathcal{E} -space is conceptually similar to that of resonant relaxation in L -space: a systematic drift that overwhelms the diffusion induced by two-body effects.) Thus tidal capture effectively increases the value of L_{min} (by a factor of ≈ 1.5 ; Novikov et al. 1992); the result is a further doubling of the stellar disruption rate. Since this gas is, on average, tightly bound to the hole, the increase in accretable gas will be even greater. This further improves the ability of the loss cone to power at least low-level activity in galactic nuclei.

How important a role will resonant tidal disruption play in normal galactic nuclei? Table 2 lists the nuclear properties of several black hole candidates, including estimates of the critical radius, r_{crit} , and the cluster mass fraction at that location, μ_{crit} . The table suggests that typical galactic nuclei are non-resonant at their critical radii (recall that resonant effects dominate only for mass fractions $\mu \lesssim 0.1$); resonant enhancement to the *overall* disruption rates in these nuclei will therefore be quite small. At radii a few times smaller than r_{crit} , however, most galaxies in the table *are* dominated by resonant relaxation, and these regions can be resolved in several instances. Because erosion of the density cusp inside r_{crit} progresses so slowly, however (see § 1.2), its detection is unlikely even after accounting for resonant effects. We therefore conclude that resonant tidal disruption will not visibly alter nuclear density profiles at currently accessible angular resolutions.

Another astrophysical system in which resonant loss cone effects are important is the Oort cloud. Although several processes contribute, the dynamical evolution of Oort cloud comets in the outer Solar System ($r \sim 10^4$ AU) is controlled mainly by the Galactic tidal field (Wiegert & Tremaine 1997; Heisler & Tremaine 1986). The tidal perturbation to the nearly-Keplerian potential of the Solar System resonantly relaxes the angular momentum of the comet orbits, occasionally removing so much of it that the comets plunge into the inner Solar System, where they may become visible as long period comets. The loss cone in this

situation arises from the ability of the giant planets (particularly Jupiter and Saturn) to scatter incoming comets onto either hyperbolic or relatively tightly bound orbits—in either case causing the comets to be “lost” from the Oort cloud. As for nuclear clusters around MBHs, the rate at which comets reach the scattering loss cone—as well as the equilibrium Oort cloud distribution function at small L (which directly determines the frequency of ‘new’ long period comets)—is set by resonant loss cone dynamics.

The relative difficulty of the numerical calculations highlights the generic advantage of using a continuum approach in this class of problems, and indicates that the development of a resonant Fokker-Planck formalism certainly merits further attention. The inherently non-linear nature of resonant relaxation and the associated complexity of its analytic description, however, suggests that it is likely to be a highly non-trivial undertaking! Further exploration of this issue is beyond the scope of this paper.

We thank Scott Tremaine for helpful discussions and a careful reading of the manuscript. This work was supported by NSERC and a Jeffrey L. Bishop Fellowship to K. R.

A. Semi-Relativistic Symplectic Integration

As discussed in § 3.2, some simulations incorporated relativistic corrections to the test stars’ orbital motion to determine the hole masses for which resonant tidal disruption is shut off by relativistic precession. Operationally this was accomplished by replacing the Kepler stepper normally used in the MVS integration scheme, which solves for motion in the Newtonian one-body problem, with a Schwarzschild stepper approximating the motion around a Schwarzschild (i.e., non-rotating) black hole. In this appendix we describe the construction of the Schwarzschild stepper itself.

In the Newtonian case all five orbital elements—the semi-major axis, a , eccentricity, e , inclination, i , argument of periapse, ω , and argument of the ascending node, Υ —are constants of the motion; hence orbits are closed and do not precess in the absence of perturbations. In the Schwarzschild case, continued spherical symmetry (which ensures that the orbital motion is planar) combined with energy and (scalar) angular momentum conservation imply that four of these elements— a , e , i , and Υ —remain constant and well-defined even for highly relativistic orbits; ω , however, is *not* fixed but precesses by an amount $\Delta\omega \approx 6\pi/[a(1 - e^2)]$ rad per orbit in the weak field limit. (The exact expression is $\Delta\omega = 2[\beta K(\beta^2\delta e) - \pi]$, where $\delta = 1/[a(1 - e^2)]$, $\beta = 2/[1 - 2\delta(3 - e)]^{1/2}$, and $K(m)$ is the complete elliptic integral of the first kind.)

Table 1. Resonant and Non-Resonant Tidal Disruption Rates

$\mathcal{E}/\mathcal{E}_{\text{crit}}$	$L_{0,\text{nr}}^{\text{a}}$	$L_{0,\text{res}}^{\text{a}}$	$L_{\text{max}}^{\text{a}}$	$\Delta L_{\text{orb}}^{\text{a}}$	$\Delta L_{\text{prec}}^{\text{a}}$	$\lambda_0 \times 10^7$	$\lambda_{\text{nr}} \times 10^7$	$\lambda_{\text{res}} \times 10^7$
8	2.8	8	125	0.022	~ 3	0.06	0.18(0.04)	5.5(1.3)
3	8	23	205	0.14	~ 6	0.8	1.4(0.2)	9(1.5)
1	23	32	354	0.80	~ 12	~ 25	18(2)	35(6)
0.3	64	91	614	5.5	~ 24	26	26(1.1)	26(1.8)

^a In units of L_{min} .

Table 2. Loss Cone Properties of Nearby Black Hole Candidates

Galaxy	D (Mpc)	M_8	ρ_6^{a}	n^{a}	r_{crit} (")	r_{crit} (pc)	μ_{crit}
Milky Way	0.01	0.025	1	1.8	7	0.3	0.3
M32	0.7	0.02	0.2	2	0.1	0.4	0.3
M31	0.7	0.3	0.1	1	1.5	5	0.4
NGC 3377	9.9	0.8	0.2	1.3	0.25	12	2
NGC 3115	8.4	20	0.6	1.75	8	350	4
M87	15.3	30	0.01	1.2	8	650	4

^a $\rho_{\star}(r) = 10^6 \rho_6 (r/1 \text{ pc})^{-n} M_{\odot} \text{ pc}^{-3}$

A Kepler stepper advances the orbital position \boldsymbol{x} and velocity \boldsymbol{v} by a time Δt through solution of some form of Kepler’s Equation, which determines the orbital phase as a function of time. The standard form of Kepler’s Equation for elliptical orbits is

$$M = E - e \sin E, \quad (\text{A1})$$

where $M = 2\pi(t - t_p)/t_{\text{orb}}$ is the mean anomaly, E is the eccentric anomaly (related to the radius by $r = a(1 - e \cos E)$), t_p is a time of pericentric passage, and $t_{\text{orb}} = 2\pi a^{3/2}$ is the orbital period. Conceptually, a relativistic geodesic stepper advances the 4-position \boldsymbol{X} and 4-momentum \boldsymbol{P} over some interval of coordinate time Δt ; however, since the Schwarzschild metric is static it is sufficient in this case to use just the 3 spatial components of position and momentum (or velocity) to advance orbits, even ones passing near the horizon. One practical disadvantage of using the true relativistic 3-velocity is that calculation of the orbital elements requires setting up and solving a cubic polynomial, which is time-consuming (as it must be redone every time step). For this reason we created a ‘semi-relativistic’ Schwarzschild stepper which returns the true orbital 3-position but an effective 3-velocity for which application of the simpler Newtonian formulae yield the correct (relativistic) orbital elements; in the weak field limit, both of these vectors become identical to their non-relativistic counterparts \boldsymbol{x} and \boldsymbol{v} . Our semi-relativistic stepper can thus be used as an exact replacement for the Kepler stepper in the integration of moderately-relativistic orbits.

Implementing a Schwarzschild stepper requires an analog of Kepler’s Equation which is valid for relativistic orbits; generalized expressions for t_{orb} and the true anomaly, ν (defined as the physical angle traversed in the orbital plane since periaipse), are also needed. Rauch (1997) has derived these formulae for orbits in the Kerr (rotating black hole) spacetime accurate to second order in δ (see above), assuming $\delta \ll 1$. For Schwarzschild the results (with errors $O(\delta^3)$) simplify to

$$t_{\text{orb}} = 2\pi a^{3/2} \left\{ 1 + \left(\frac{3}{a}\right) \left[1 + \left(2 + \frac{5}{2}\sqrt{1 - e^2}\right) \delta \right] \right\}, \quad (\text{A2})$$

$$\nu(\chi) = \left\{ 1 + 3\delta + [54 + 3e^2] \frac{\delta^2}{4} \right\} \chi + \left\{ 1 + \left[9 + \frac{3}{4}e \cos \chi \right] \delta \right\} \delta e \sin \chi, \quad (\text{A3})$$

and $M = E - \tilde{e} \sin E + \Delta E$, where $\Delta E = \frac{15}{2}(\chi - E)(1 - e^2)^{3/2}\delta^2$ and

$$\tilde{e} = e \left\{ 1 - \left(\frac{3}{a}\right) \left[1 + \left(-10 + 18e^2 + 15\sqrt{1 - e^2}\right) \frac{\delta}{6} \right] \right\}. \quad (\text{A4})$$

Here χ is the ‘relativistic anomaly,’ defined according to $r = a(1 - e^2)/(1 + e \cos \chi)$ —hence χ advances by exactly 2π from one periaipse to the next, regardless of the amount of orbital precession (which is $\Delta\omega = \nu(2\pi) - 2\pi \approx 6\pi\delta$, in agreement with the value given above);

for strictly Keplerian orbits (i.e., $\delta \rightarrow 0$), $\chi = \nu$. Note that since $0 \leq \tilde{e} < e < 1$, the modified Kepler’s Equation can be solved economically by finding the solution for $\Delta E \rightarrow 0$ and then correcting for the finite value of ΔE . We found the resulting stepper to be only a factor of two slower than its Newtonian counterpart and to give excellent results (compared to accurate integrations of the Schwarzschild problem) for radii $r \gtrsim 10$, at which point the systematic error in the precession rate was $\approx 25\%$.

B. Chaos in MVS Integration of Nearly-Radial Orbits

By construction the MVS integration scheme (see § 2.4) is exact in the limit of unperturbed Keplerian motion. As a symplectic mapping, the method might also be expected to be free of systematic, long-term growth of energy error in the slightly perturbed problem (i.e., for nearly-Keplerian motion)—this property being one of the key advantages of such algorithms. Applied to our simulations, however, the MVS integrator was found to exhibit unbounded error growth even for very small perturbations, in some cases causing test star orbits to become unbound in as few as 100 orbital periods (the physical energy relaxation timescale being orders of magnitude longer). As we explain below, the instability is related to the very high eccentricities of the test star orbits; qualitatively similar integrations (e.g., tracing the orbital evolution of Oort cloud comets) are therefore likely to suffer from the same problem. In this section we briefly discuss the problem, and propose a modified integration scheme which remains robust under such circumstances.

Our integrations are somewhat unique for two reasons: the test star orbits are all highly eccentric (generally, $e \gtrsim 0.999$), and the perturbations from the background cluster are very nearly constant over scales of order the pericentric distance—the perturbations are spatially well-resolved with a stepsize $\Delta t/t_{\text{orb}} \sim 10^{-3}$, taking the form of a small, fixed tidal force near periapse. Hence there is no *a priori* reason to integrate using a stepsize small enough to resolve periapse ($\Delta t/t_{\text{orb}} \sim (1 - e)^{-3/2} \sim 10^{-5}$), which would be impractical in any case—recall that symplectic integrators do not easily admit variable stepsizes; this is (in principle!) the great advantage of the MVS method for nearly-Keplerian problems. For stepsizes not resolving periapse, however, it was found that significant jumps in the energy, centered around periapse, occurred each orbit. This produced a linearly growing energy error—even in simulations where the background masses were held fixed, for which energy should be strictly conserved. In our case, it was possible to work around the problem by artificially truncating the cluster at a relatively large radius— $\sim a/30$ for test stars with semi-major axis a —for which the residual tidal force at periapse was small enough that physical energy relaxation dominated that spuriously produced by the MVS method;

angular momentum relaxation is nearly unchanged as it is controlled by the largest-scale fluctuations in the background cluster. Although this proved adequate, it would be more elegant (and generically more useful) to modify the MVS scheme so that it did not suffer from this problem; although a detailed treatment is beyond the scope of this paper, we will mention one possible solution.

Since the perturbing force is almost constant near periapse—where effectively all of the erroneous relaxation occurred—an excellent model analogy to our situation is provided by the Stark problem, in which the perturbing force is strictly constant in magnitude and direction over the entire orbit. Besides its simplicity, the Stark problem has the added advantages of being integrable and having a conserved energy; this guarantees that any energy relaxation or chaotic behavior found in numerical integrations of the problem are an artifact of the integrator itself. Sample integrations using the MVS scheme confirmed that for stepsizes resolving periapse, there was no systematic growth in the energy error, as nominally expected from a symplectic scheme; unresolved orbits, on the other hand, generally had erratic, unbounded growth of energy error, even for extremely small perturbations. More direct (though informal) evidence for dynamic chaos in the integrator was found in the sensitivity of the relaxation curves to the precise initial conditions used, which was not present in the stable integrations.

The close correspondence between the Stark problem and our simulations suggests that a more robust integrator might result by replacing the Kepler stepper used in the MVS method with a Stark stepper solving that problem exactly (which can be done in parabolic coordinates using elliptic functions and integrals). In contrast to the standard MVS scheme, which is exact in the limit of zero perturbations, the Stark integrator is exact in the limit of a constant (possibly large) perturbation force. A brief investigation revealed that the new method, as expected, does not suffer from the aberrant relaxation present in MVS scheme—even for large stepsizes that do not resolve the passage through periapse. On the other hand, the practicality of a Stark integrator depends on the speed of the Stark stepper itself, which will be much slower (and more tedious to implement) than the Kepler stepper it replaces. Based on the encouraging initial tests, an efficient implementation of the proposed Stark integrator is currently being undertaken; detailed results will be reported elsewhere.

REFERENCES

- Bade N., Komossa S., Dahlem M., 1996, *A&A*, 309, L35
Bahcall J. N., Wolf R. A., 1976, *ApJ*, 209, 214

- Carter B., 1992, ApJ, 391, L67
- Carter B., Luminet J.-P., 1983, A&A, 121, 97
- Cohn H., Kulsrud R. M., 1978, ApJ, 226, 1087
- Danby J. M. A., 1992, Fundamentals of Celestial Mechanics. Willmann-Bell Inc., Richmond
- Diener P., Kosovichev A. G., Kotok E. V., Novikov I. D., Pethick C. J., 1995, MNRAS, 275, 498
- Duncan M. J., Shapiro S. L., 1983, ApJ, 268, 565
- Eckart A., Genzel R., 1996, Nature, 383, 415
- Eracleous M., Livio M., Binette L., 1995, ApJ, 445, L1
- Eracleous M., Livio M., Halpern J., Storchi-Bergmann T., 1995, ApJ, 438, 610
- Evans C. R., Kochanek C. S., 1989, ApJ, 346, L13
- Frank J., 1978, MNRAS, 184, 87
- Frank J., Rees M., 1976, MNRAS, 176, 633
- Grupe D., Beuermann K., Mannheim K., Bade N., Thomas H.-C., de Martino D., Schwöpe A., 1995, A&A, 299, L5
- Heisler J., Tremaine S., 1986, Icarus, 65, 13
- Hills J. G., 1975, Nature, 254, 295
- Hills J. G., 1988, Nature, 331, 687
- Hills J. G., 1991, AJ, 102, 704
- Khokhlov A., Melia F., 1996, ApJ, 457, L61
- Kinoshita H., Yoshida H., Nakai H., 1991, Cel. Mech., 50, 59
- Kochanek C. S., 1994, ApJ, 422, 508
- Kormendy J., Richstone D., 1995, ARA&A, 33, 581
- Kormendy J. et al., 1996, ApJ, 459, L57
- Laguna P., Miller W. A., Zurek W. H., Davies M. B., 1993, ApJ, 410, L83

- Lauer T. R. et al., 1996, AJ, 110, 2622
- Lightman A. P., Shapiro S. L., 1977, ApJ, 211, 244
- Lin D. N. C., Tremaine S., 1980, ApJ, 242, 789
- Luminet J.-P., Barbuy B., 1990, AJ, 99, 838
- Lynden-Bell D., 1969, Nature, 223, 690
- McMillan S. L. W., Lightman A. P., Cohn H., 1981, ApJ, 251, 436
- Novikov I. D., Pethick C. J., Polnarev A. G., 1992, MNRAS, 255, 276
- Quinlan G. D., Hernquist L., 1997, preprint
- Quinlan G. D., Hernquist L., Sigurdsson S., 1995, ApJ, 440, 554
- Rauch K. P., 1997, ApJ, submitted
- Rauch K. P., Tremaine S., 1996, NewA, 1, 149
- Rees M., 1988, Nature, 333, 523
- Roos N., 1992, ApJ, 385, 108
- Shapiro S. L., Marchant A. B., 1978, ApJ, 225, 603
- Spitzer L., Hart M. H., 1971, ApJ, 164, 399
- Stoeger W. R., Pacholczyk A. G., Stepinski T. F., 1992, ApJ, 391, 550
- Storchi-Bergmann T., Eracleous M., Livio M., Wilson A., Filippenko A., Halpern J., 1995, ApJ, 443, 617
- van der Marel R. P., de Zeeuw P. T., Rix H.-W., Quinlan G. D., 1997, Nature, 385, 610
- Wiegert P., Tremaine S., 1997, Icarus, submitted
- Wisdom J., Holman M., 1991, AJ, 102, 1528
- Young P. J., 1977, ApJ, 215, 36